

Extending the Dynamic Range of Electronics in a Time Projection Chamber

J. Estee^{a,b}, W.G. Lynch^{a,b}, R. Wang^{j,k}, J. Barney^{a,b}, G. Cerizza^{a,b}, B. Hong^c, T. Isobe^d, G. Jhang^b, M. Kaneko^e, M. Kurata-Nishimura^d, P. Lasko^f, J. W. Lee^c, J. Łukasik^f, A.B. McIntosh^g, T. Murakami^e, P. Pawłowski^f, K. Pelczarⁱ, C. Santamaria^b, D. Suzuki^d, M. B. Tsang^b, S.J. Yennello^g, Y. Zhang^h, and the S π RIT collaboration

^a*Dept. Physics and Astronomy, Michigan State University, East Lansing, Michigan, 48824, USA*

^b*National Superconducting Cyclotron Laboratory, East Lansing, Michigan, 48824, USA*

^c*Department of Physics, Korea University, Seoul 136-703, Republic of Korea*

^d*RIKEN Nishina Center, Hirosawa 2-1, Wako, Saitama 351-0198, Japan*

^e*Department of Physics, Kyoto University, Kita-shirakawa, Kyoto 606-8502, Japan*

^f*Institute of Nuclear Physics PAN, ul. Radzikowskiego 15231-342 Kraków, Poland*

^g*Dept. of Physics and Astronomy, Texas A&M University, College Station, TX 77843, USA*

^h*Department of Physics, Tsinghua University, Beijing 100084, P. R. China*

ⁱ*Faculty of Physics, Astronomy and Applied Computer Science, Jagiellonian University, ul. Gołębia 24, 31-007 Kraków*

^j*State Key Laboratory of Radiation Medicine and Protection, School of Radiation Medicine and Protection, Soochow University, Suzhou 215123, China*

^k*Collaborative Innovation Center of Radiological Medicine of Jiangsu Higher Education Institutions, Suzhou 215123, China*

Abstract

When Time Projection Chambers (TPCs) are used in low to intermediate nuclear collisions, the mass and momentum range covered by the emitted particles cover a wide range in energy losses. Many TPC readout electronics currently only have a single gain output with a fixed dynamic range. In a recent set of experiments using the SAMURAI Pion-Reconstruction and Ion-Tracker (S π RIT) TPC, it was important to simultaneously measure relativistic pions and heavy ion tracks from the same collisions. As a tracks energy loss is collected and multiplied by the anode wires, a distribution of image charges are induced on the TPC read out pads. If the avalanche on a wire is large enough, the charge collected on a pad will saturate the electronics, though only for pads directly underneath the avalanche; pads further away in the distribution will not be saturated. Using these unsaturated pads and the known distribution function,

we can estimate the saturated pads, increasing the dynamic range by a factor of 10.

Keywords: `elsarticle.cls`, L^AT_EX, Elsevier, template

2010 MSC: 00-01, 99-00

1. Introduction

Charged particles emitted in low to intermediate energy nuclear collisions cover a large range in energy losses from very small energy losses, for minimum ionizing particles, to much higher energy losses, for slower moving, heavy fragments. Figure 1 shows the range of momenta typically observed in intermediate energy collisions, around 300 MeVA, and the energy loss range involved.

Measuring the full range in energy losses have motivated the development of large dynamic range electronics, which are able to switch between high and low gains covering a very large dynamic range; however, many current Time Projection Chambers (TPCs) readout electronics have a single gain output, presenting a problem for the readout of such devices.

Several techniques have been employed to increase the dynamic range for energy losses in TPCs. In the EOS TPC [1], a larger dynamic range was achieved by lowering the voltage on selected anode wires, decreasing the gas amplification on those wires. In the prototype Active Target TPC (PAT-TPC) an equivalent reduction in gain was achieved by lowering the electronics gain for some of the readout channels. me sections, and optimizing the gain for strongly ionizing particles in others. For strongly ionizing particles, lowering the gain improves the momentum resolution, while worsening the dE/dx resolution, and vice versa for weakly ionizing particles.

These strategies have drawbacks in applications where the experiment's requirements cannot accept the associated degradation in the dE/dx resolution, or the momentum resolution. Finding the solution to this problem has motivated the development of software based analysis that will extend the dynamical range of TPCs; we illustrate an alternate approach to expand the dynamic

range within the context of a standard multi-wire TPC, without the need of extra hardware or dedicating regions of lower gain.

Many TPC readout electronics have a single gain output with a dynamic range (defined the ratio of the maximum signal to the electronic noise) of no more than 1000:1. In our case the maximum signal to noise was about 700:1. We required the smallest signal of minimum ionizing particles (m.i.p.) to be 20:1, setting the dynamic range to be 35 times m.i.p. Figure 1 illustrates the range in momentum we expect to see saturation effects. The shaded region shows where 35 times that of the minimum ionizing pion signal where we could expect saturation to occur. While the pion's momentum range can fully be measured, without saturation effects, heavier particles would be harder to resolve in dE/dx at lower momentum.

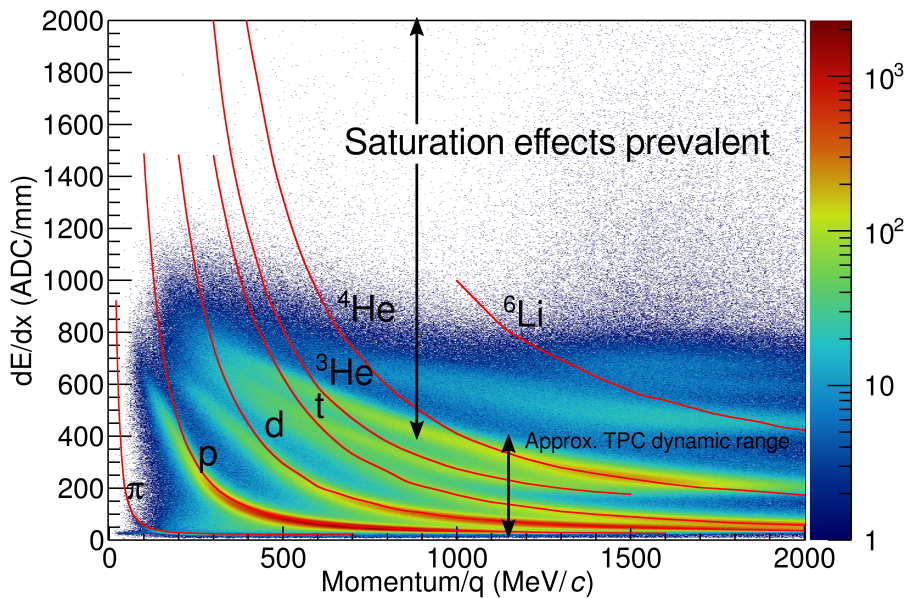


Figure 1: The expected dE/dx lines of different particles are given in red with the raw data of the S π RIT TPC in the contour plot. The effect of the electronics saturation on the PID especially at low momentum and heavy ions can be seen.

1.1 TPC Overview. We begin our discussion by describing some basic properties of the SAMURAI Pion Reconstruction and Ion-Tracker (S π RIT) TPC [2]. For

- ⁴⁰ the following discussion we have defined the $+x$ axis to point to the left of the beam, the $-y$ axis to point down into the drift volume, and the $+z$ axis to point along the beam.

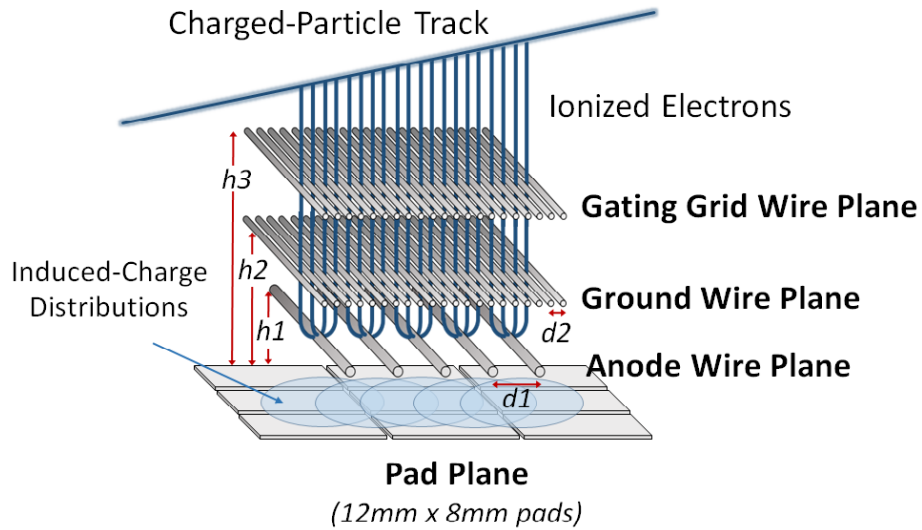


Figure 2: Cartoon graphic showing the 3 wire planes and a section of the pad plane. $h_3 = 14$ mm, $h_2 = 8$ mm, $h_1 = 4$ mm, $d_2 = 1$ mm, $d_1 = 4$ mm. This graphic is inverted from the actual wire planes and pad plane to display the perspective easier.

⁴⁵ *Pad plane.* The S π RIT TPC pad plane is composed of a rectangular charge sensitive pads, each with an x dimension of 8 mm wide, and a z dimension of 12 mm. These pads are arranged in a grid measuring 112 by 108 pads with a total area of 1344 mm \times 864 mm.

⁵⁰ *Wire planes.* As illustrated in Figure 2, the S π RIT TPC consists of three wire planes below the pad plane, with the wires aligned along the x -axis. The wire plane farthest from the pad plane (14 mm) operates as an ion-gate or a gating grid [3]. The middle wire plane (8 mm) is grounded. When the gating grid is open, electrons ionized by reaction products in the drift volume drift through both the gating grid and ground planes.

Closest to the pad plane is the high voltage, anode wire plane (4 mm),

consisting of 20 μm diameter wires spaced 4 mm apart. In the vicinity of
55 these wires an avalanche occurs multiplying the secondary electrons drifting up
from the drift volume, created from the track's energy loss in the detector gas.
When these secondary electrons reach the anode wires, they are amplified on
the order of 1000 times creating electron and ion pairs. It is the motion of these
slow moving ions, as they drift away from the anode wires, that induces image
60 charges on the read out pads above. The distribution of image charged on the
pad plane is centered about the avalanche region on the wires and its width is
fixed by the distance from the pad plane.

The anode wires are sectioned off into 14 independent sections, each containing 26 wires; 12 sections were biased to 1460 V. This setting was optimized
65 to ensure m.i.p. particles such as pions would have a signal to noise ratio of
around 20:1. The two remaining sections were biased to 1214 V due to high
current issues, reducing the gas gain by a factor of 10 times as compared to the
other anode sections. As demonstrated by the EoS TPC [1], lowering the anode
wires effectively extended the dynamic range. This gain reduction allowed for
70 a direct validation of the success of the new method for extending the dynamic
range presented here.

Generic Electronics for TPCs. Signals in the S π RIT TPC are amplified and
digitized by the recently developed Generic Electronics for TPCs (GET) [4].
Short cables transmit the signals from the pads to the inputs of the AGET chips.
75 Each AGET chip services 64 pads (63 pads are connected in our case), contains
a pre-amplifier, and a Switched Capacitor Array (SCA), with a maximum of
512 time buckets with an adjustable sampling frequency of 1 to 100 MHz. Four
AGET chips are mounted on one AsAd (ASIC and ADC) motherboard. The
gain of each AGET can be configured as 0.12, 0.24, 1.0, or 10 pC over the whole
80 dynamic range, and the ADCs on each AsAd board provides 12 bit resolution.
The peaking times of the shaping amplifiers can be set to 69, 117, 232, 501,
720, or 1014 ns. In this experiment, the gain was set to the highest setting, 0.12
pC, the peaking time 117 ns, and the sampling frequency 25 MHz (resulting in

40 ns time buckets). The Aget 2.0, asad 2.1, and cobo 1.0 firmware versions
85 were used. The variations in the electronics were calibrated by measuring the response of each channel to a injected reference pulse, covering the full dynamic range of each channel.

Analysis Software. The S π RITROOT software is modular tasked based code based on the FAIRROOT package written in C++ [5]. The main tasks in the
90 S π RITROOT software reconstruction are:

- Decoder task
- Pulse Shape Algorithm (PSA Task)
- Helix Track Finding Algorithm
- Clustering Algorithm
- Track Fitting (GENFIT package)
95
- Vertex Fitting (RAVE package)

The decoder task converts the binary data file into a container class which maps the electronics channels into the corresponding pads and (x,z) coordinates.

There may be several pulses in a pad coming from two tracks passing under
100 the same pad separated by arrival time. Using an expected pulse shape the PSA task fits the signal pulses within a pad, giving the arrival time of the drifted electrons from each particular track. The height of the fitted pulse is proportional to the total charge of that event, Q and the y-coordinate is calculated as $y = v \cdot t_0$ where v is the drift velocity and t_0 the arrival time.
105 Combining the information from these first two tasks, (x,y,z,Q), we construct what is called a "hit".

The Helix Track Finding Algorithm finds the collection of hits belonging to one track out of all the hits in an event. The hits within a track are then reduced into clusters. A cluster's position is the average position of the hits within a cluster, with the total charge of the cluster being the sum of the hits charges.
110

A tracks average position is estimated by the cluster's average position. The clusters are then fitted in the GENFIT track fitting package [6], giving the final momentum of the track. A final vertex of the event is fitted from all tracks using the package RAVE [7].

115 *Definition of clustering.* A brief description of the method of clustering is illustrated in Figure 3. It is impractical to cluster in both the x and z-axis and we only cluster the hits along one axis. The three clusters at the bottom of Figure 3 are clustered along the x-axis and the upper three are along the z-axis, as shown by the bolded pads for one of the clusters in each direction.

120 The clustering direction depends on the angle of the track with respects to the x-axis, defined as θ . For example, a track going along the z-axis the crossing angle is defined as 90° , and a track going along the x-axis defined as 0° . In the case that the crossing angle is $45^\circ < \theta \leq 90^\circ$ the clustering direction is along the x-axis. For $0^\circ < \theta \leq 45^\circ$ it is along the z-axis.

125 The position along the clustering direction is calculated by weighting the individual hit's positions by their charges q_i and getting the mean value. The other direction is set to the center of the pad. For example if we are clustering along the x-axis for a cluster, the z-position is set to the center of the pad in the z-direction and vice versa.

130 Clustering in this way gives us better position resolution for calculating the position of each cluster. You could imagine if we calculated the clusters only along the x-axis for tracks with $\theta \approx 0^\circ$ the x-position is not well defined. By clustering in the direction most perpendicular to the track, we get a better position resolution.

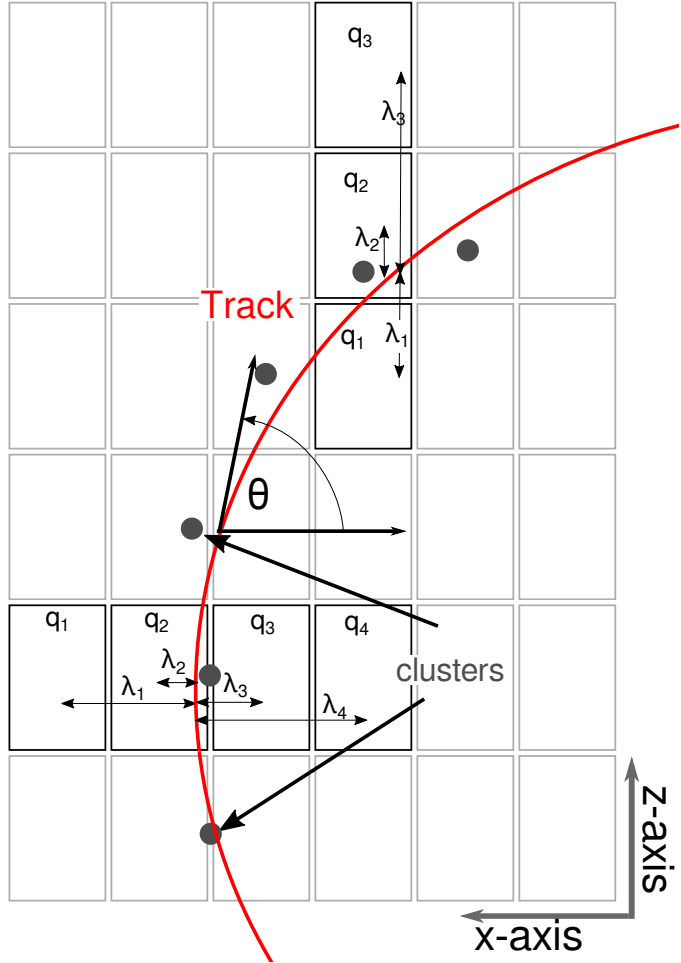


Figure 3: Cartoon graphic of a top down view of a fit to a track passing through several pads. The bolded pads and the charges q_i represent the hits belonging to that pad and the clusters of the track representing the average position of the track. The three clusters at the bottom are clustered in the x-direction and for the upper three clustered in the z-direction. The estimate of the position of the avalanche is given by the track fit and the position from the center to each pad to the \bar{x} position is given as λ_i .

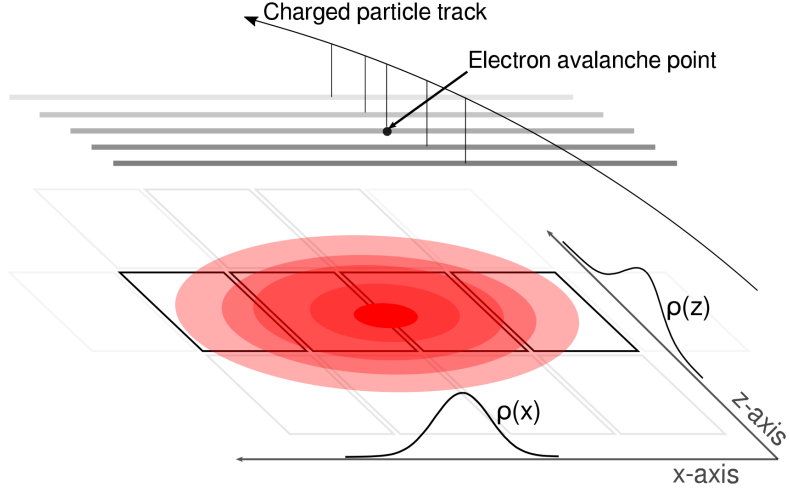


Figure 4: A cartoon illustration of the charge distribution resulting from an electron avalanche on one wire and the projections of the distribution onto the two axis $\rho(x)$ onto the x-axis and $\rho(z)$ onto the z-axis. The orientation of the wire planes is flipped upside down to display the perspective better.

¹³⁵ 2. Pad Response Function

As illustrated in Figure 4 the distribution resulting from an electron avalanche is 2-dimensional, with the charge observed on each pad being the integral of that distribution over the pad's dimensions; also called the Pad Response Function (PRF). The projection onto the x and z-axis of this distribution is shown as ¹⁴⁰ $\rho(x)$ and $\rho(z)$.

In this example the clustering direction would be along the x-axis, as illustrated by the bolded pads. By choosing to clustering only in one direction, we have not included the charge in adjacent pads along the z-axis resulting from the tails of $\rho(z)$. Therefore the charge not included in the the bolded pads will be ¹⁴⁵ included in adjacent clusters, introducing small correlations in charge between neighboring clusters.

Gatti Pad Response Function. Gatti [8] expressed a semi-empirical equation for the charge distribution in a simple multi-wire TPC such as that found in the

S π RIT TPC. Given in Eq. 1, the function depends only on the width of a pad
150 (w), height of the anode plane to the pad plane (h), and the distance of the pad center to the avalanche point λ . It is a single parameter equation where the two parameters $K_1 = \frac{K_2\sqrt{K_3}}{4\text{atan}(\sqrt{K_3})}$ and $K_2 = \frac{\pi}{2} \left(1 - \frac{\sqrt{K_3}}{2}\right)$ depend on the parameter K_3 , which is a function of the ratio of the anode wire diameter to the height of the anode wires to the pad plane. K_3 can be looked up in a graph in [9] and [8].

$$\begin{aligned} PRF_{gatti}(\lambda) &= \frac{K_1}{K_2\sqrt{K_3}} [\arctan(\sqrt{K_3}\tanh[K_2(\frac{\lambda}{h} + \frac{w}{2h})]) \\ &\quad - \arctan(\sqrt{K_3}\tanh[K_2(\frac{\lambda}{h} - \frac{w}{2h})])] \end{aligned} \quad (1)$$

155 *Experimental PRF.* The correlations we introduced by only clustering along one direction do not play a significant role in the particle identification, but cause deviations from the expected Gatti distribution. Also, analytic PRFs only exist for classical multi-wire TPCs. For these reasons it is useful to experimentally measure the PRF and fit it with some empirical function, typically a Gaussian,
160 to describe its behavior.

As shown in Figure 3, we postulate that the PRF is a function of the total charge deposited in a cluster $Q = \sum_i q_i$ and the difference in position of the center of the i^{th} pad, x_i , to the mean position $\bar{x} = \sum_i x_i q_i / Q$, which we call $\lambda_i = x_i - \bar{x}$. The PRF is simply defined as the charge fraction of each pad as a
165 function of λ , Equation 2.

$$PRF(\lambda_i) = \frac{q_i(\lambda_i)}{Q} \quad (2)$$

Averaging over many events in the experimental data, the resulting PRF for the S π RIT TPC is shown in Figure 5. Here we see the deviations from the expected analytic Gatti distribution where as fitting with a two parameter Gaussian function describes the data better. With the two parameters being
170 the normal coefficient, N_0 , sigma σ , and with a mean value assumed to be 0 as given in Equation 3.

$$PRF_{gaus}(\lambda) = N_0 e^{\frac{-\lambda^2}{2\sigma^2}} \quad (3)$$

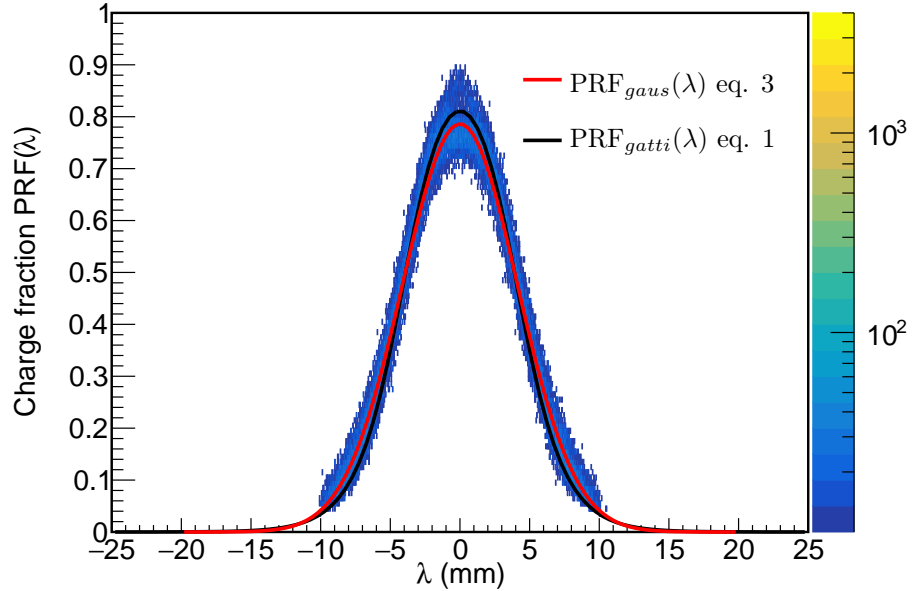


Figure 5: Experimental pad response function of many events for a crossing angle of $85^\circ < \theta \leq 90^\circ$.

3. PRF vs crossing angle

The shape of the PRF depends on the crossing angle [8]. As plotted in Figure 6 is the PRF of a π^- tracks vs the crossing angle θ . One can see the PRF gets wider going from 90° to 45° . Once could imagine if we did not switch clustering directions the PRF would become wider until it was a uniform distribution and there was no position resolution. Since we switch the clustering direction from x to z at 45° , the opposite trend is seen where the PRF becomes narrower going from 45° to 0° .

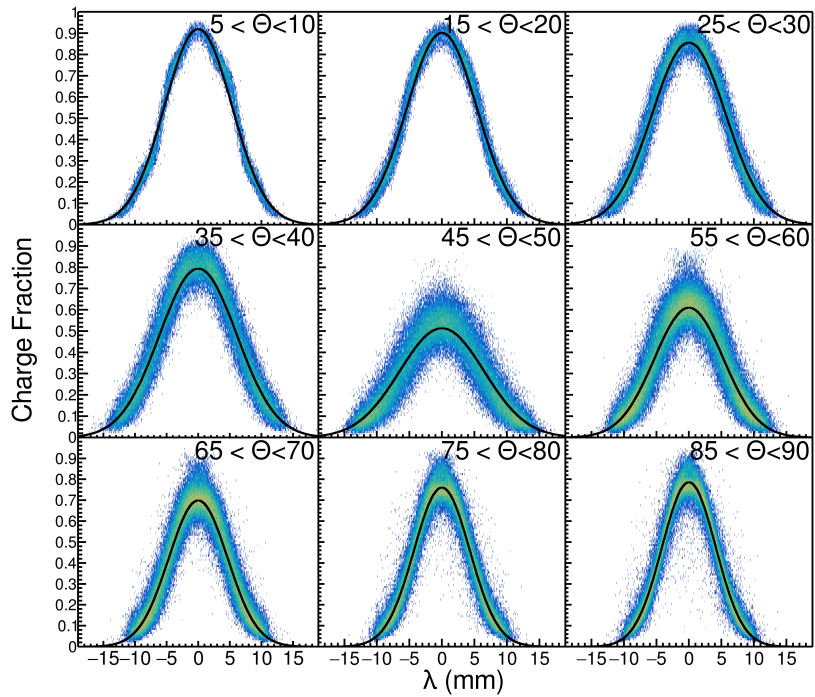


Figure 6: Experimental pad response function as a function of the crossing angle θ

| Coefficient | c_0 | c_1 | c_2 | c_3 | c_4 |
|--------------------|--------|-----------|-----------|-----------|----------|
| $0 < \theta < 45$ | | | | | |
| N_0 | .897 | 5.766E-3 | -4.263E-4 | 7.444E-6 | 5.705E-8 |
| σ | 5.496 | -3.920E-2 | 2.693E-3 | -5.208E-5 | 5.334E-7 |
| $45 < \theta < 90$ | | | | | |
| N_0 | 1.220 | -6.258E-2 | 1.608E-3 | -1.492E-5 | 4.654E-8 |
| σ | 31.368 | -1.109 | 1.779E-2 | -1.336E-4 | 3.940E-7 |

Table 1: Coefficients of the 4 th order polynomial fit to the Gaussian parameters N_0 and σ . The polynomial form is given as $c_0 + c_1x + c_2x^2 + c_3x^3 + c_4x^4$

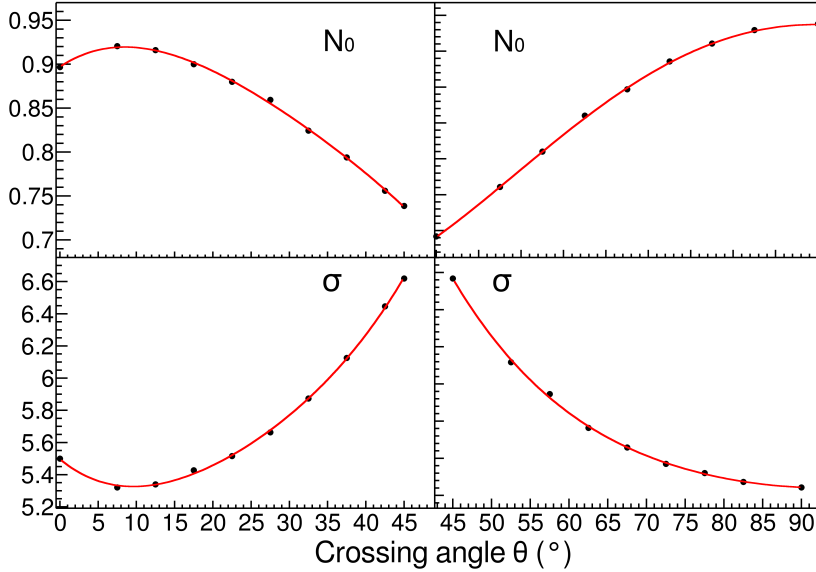


Figure 7: Parameters N_0 and σ as a function of the crossing angle θ with the 4 th order polynomial fits given in Table 1.

Fit's were performed to the experimental data binning 5° width bins from $0^\circ < \theta \leq 90^\circ$. The two parameters of the Gaussian fits are plotted versus θ in Figure 7; a 4 th order polynomial fit between these points allowed for interpolating between θ ; the coefficients of the fits given in Table 1.

Method of Desaturation. We will use the term “desaturation” for our process
 185 of correcting the charge values of the saturated pads. Figure 8 shows a typical situation of saturated signals. When an avalanche causes a large induced signal, the pads directly underneath collect the largest charge becoming saturated represented by $q_{2'}$ and $q_{3'}$. Pads further away experience smaller, non saturating charges represented by q_1 and q_4 . Though we don’t know the saturated
 190 charge values, the distribution of all charges must follow the PRF which we have experimentally measured. From the clusters crossing angle, we can get the corresponding parameters for the PRF as described above in Figure 7.

We assume the distance of each pad to the track, λ_i is fixed, this defines the fraction of charge each pad receives as defined by the $PRF(\lambda_i)$ function.

195 A chi squared function, $\chi^2 = \sum_i \frac{(q_i^{obs} - q_i^{expect})^2}{q_i^{expect}}$, where q_i^{obs} are the observed, non-saturated charges q_1 and q_4 , and q_i^{expect} are the expected charges observed; calculated as $q_i^{expected} = Q \cdot PRF(\lambda_i)$. The charges, $q_{2'}$, $q_{3'}$, make up the unknown variable and are allowed to vary in the χ^2 minimization but are added to make up the total expected charge Q . The minimum of the χ^2 distribution
 200 gives best estimate for the saturated charge values on each pad.

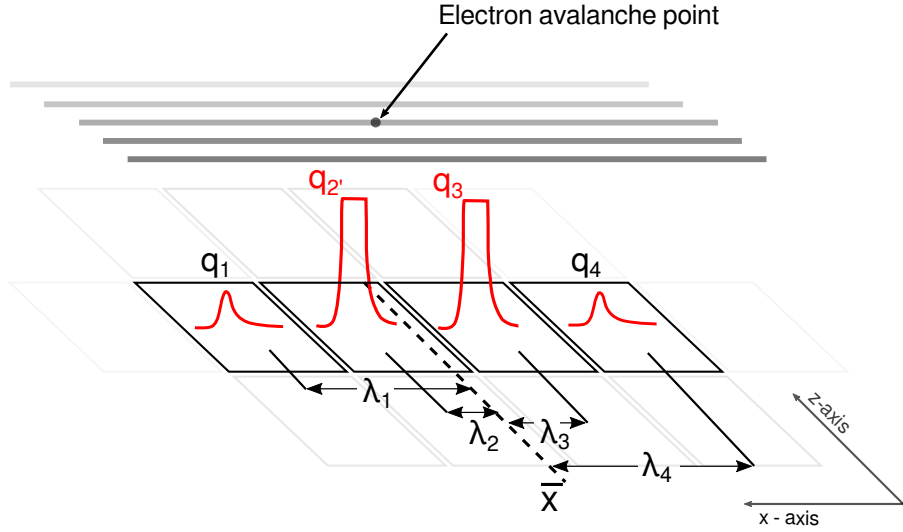


Figure 8: A typical case of a saturating event. The pads directly underneath the avalanche point, $q_{2'}$ and $q_{3'}$, are saturated while pads farther away, q_1 and q_4 are not saturated.

4. Experimental data

Two sets of data were used for the testing and validation of this method. A cocktail beam consisting of ($p, d, t, {}^3He, {}^4He, {}^6Li, {}^7Li$) light charged particles was injected into the TPC for calibration purposes, and tuned to two different 205 rigidity, $\beta\rho$, settings. The momentum resolution was approximately 1%, as determined by the slits of the BigRIPS fragment separator of the Radioactive Isotope Beam Factory (RIBF) in RIKEN. A thick 21 mm thick aluminum target was inserted for part of the lower $\beta\rho$ setting, further reducing the energy of the beam for a third calibration point.

210 In a typical cocktail event, one particle enters the TPC volume at a time and parallel to the pad plane, representing an ideal case for momentum and dE/dx determination; as it does not suffer from inefficiencies of high multiplicity events seen in the collision experimental data.

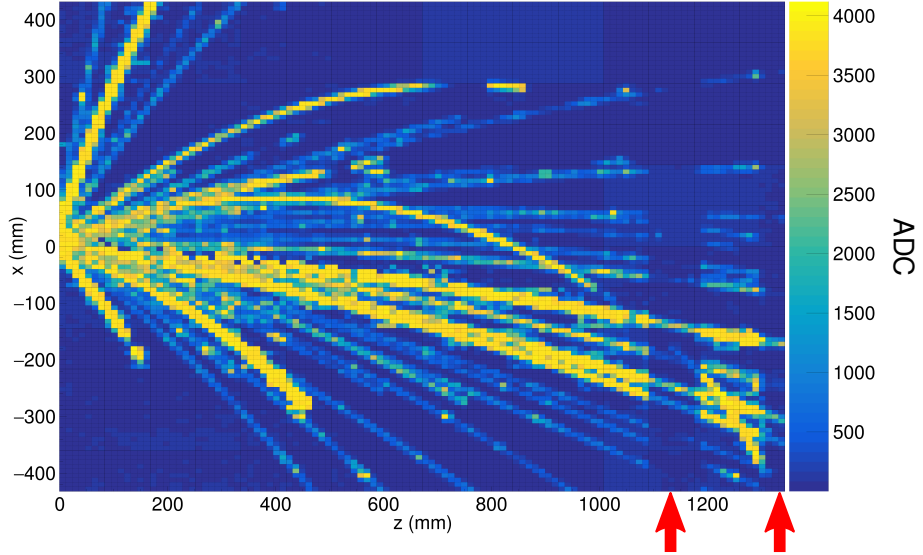


Figure 9: Pad plane projection for a collision event in the TPC. Highlighted by red arrows are two regions of anode wires which had a reduced voltage of 1214 V. The voltage of the rest of the TPC anode wires are 1460 V. The reduction in voltage reduces the gain by a factor of about 10x.

The other type of data was the collision of a ^{132}Sn beam onto a ^{124}Sn target
 215 triggered on central nuclear collisions. Shown in Figure 9 is the typical pad plane response for a central nuclear collision. During the experiment the voltages of two anode sections (as indicated by red arrows in Figure 9) were biased to 1214 V. The gain in the gain of these sections were also reduced by a factor of about 10 times, as compared with the other sections which were biased to 1460 V. We
 220 refer to the 1460 V region as high gain and the 1214 V region as low gain.

5. Results

Low gain vs corrected high gain. Tracks which saturate pads in the high gain region are not saturated in the low gain region; by comparing the dE/dx values of these two sections, we can directly measure the success of the high gain region's desaturation using the method described above.
 225

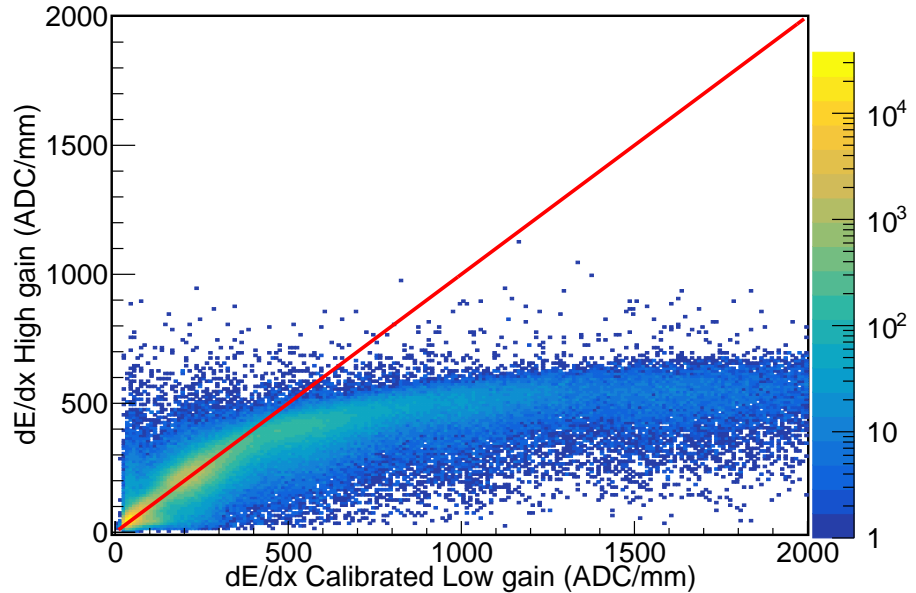


Figure 10: The uncorrected high gain dE/dx vs low gain dE/dx collision data.

In Figure 10, the effect of saturation can be seen in the high gain region for the uncorrected data. For signals below 400 ADC/mm the electronics are not saturated, and therefore the high and low gain sections agree. The data starts to saturate above 400 ADC/mm in the high gain channels eventually reaching a plateau; the low gain sections have not saturated and provide true dE/dx values.
230 After applying the desaturation method, the correlation between the high and low gain sections is restored, as seen in Figure 11. We believe the correction to at least about 2000 ADC/mm, increasing the dynamic range by a factor of 5 times.

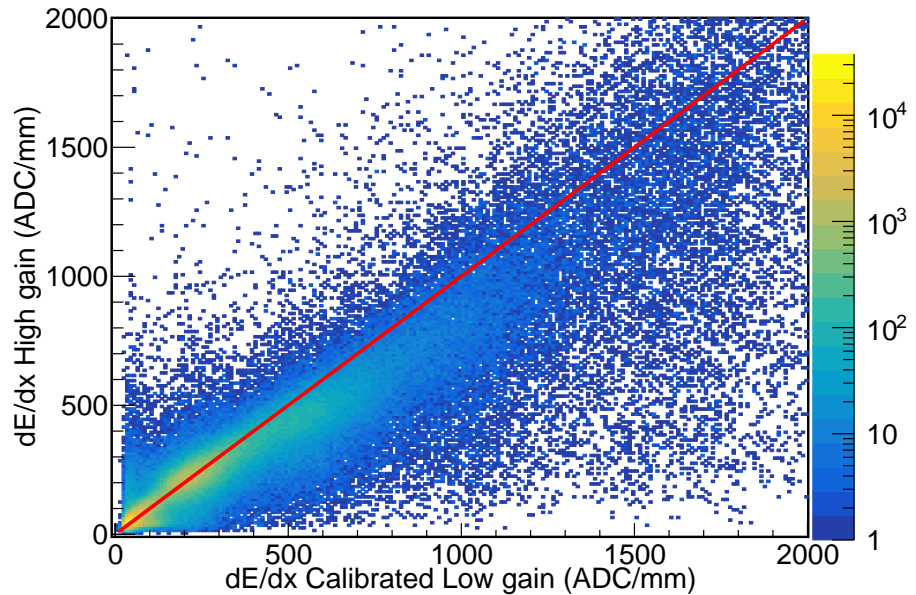
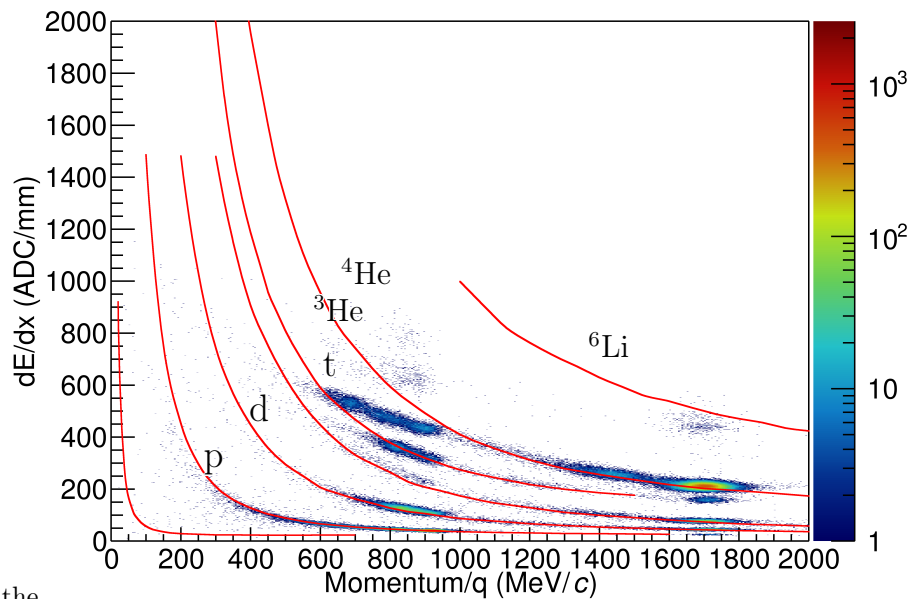


Figure 11: The corrected high gain dE/dx vs low gain dE/dx for collision data.



the

Figure 12: Uncorrected cocktail data.

235 *Particle Identification (PID).* Comparing the low to high gain sections provides
a direct measurement for determining the success of the desaturation technique,
but the goal would be to improve the particle identification (PID). In the fol-
lowing PID plots the red lines represent the most probable energy loss as given
by Geant4 straggling functions. A linear calibration was performed to convert
240 keV in Geant4 to ADC in the experiment given by $\frac{ADC}{mm} = 20 \cdot \frac{keV}{cm}$.

There are pronounced PID lines of several particle species in both the un-
corrected and corrected cocktail beam PID in figures 12 and 13. Three ovals
around 1700 and two near 900 MeV/c/Z correspond to the three $B\rho$ settings
injected into the TPC. The tails of the PID lines resulting from the particle
245 losing its initial energy, passing through the walls and other materials outside
the main detector volume; therefore lowering their initial momentum.

The uncorrected data in Figure 12 shows the effects of saturation; the PID
lines deviate from their theoretical expectations starting around 400 ADC/mm
eventually reaching a plateau. After applying the desaturation technique, we
250 see a large improvement; most notably the He and Li particles, which suffer
the most from saturation. A more subtle improvement of the lighter particles,
(p,d,t), can also be seen in the PID lines at lower momentum.

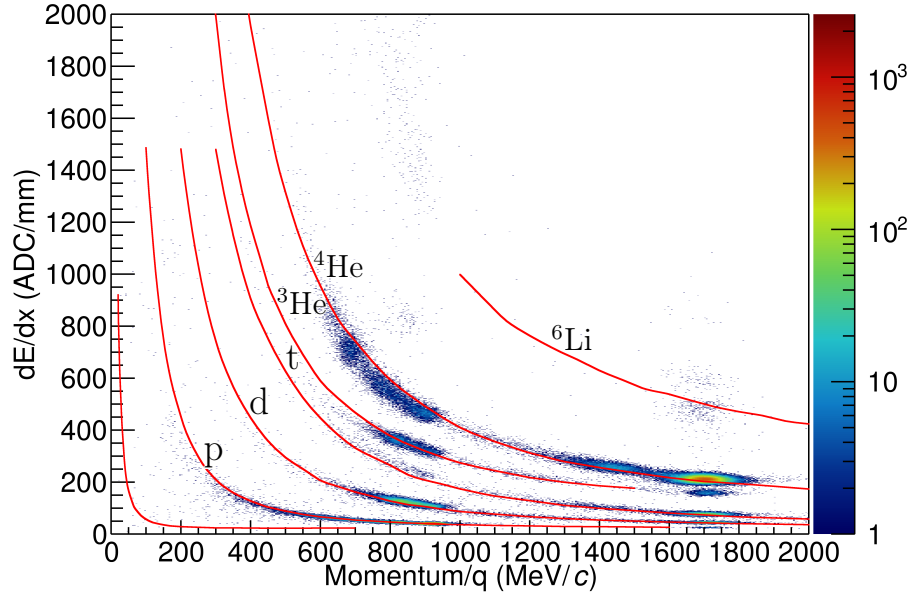


Figure 13: Corrected (desaturated) cocktail data.

Looking at the collision data, in figures 14 and 15, we also see a similar result. The collision data PID suffers from more background and inefficiencies than the cocktail beam; nevertheless we can see a similar improvement in the PID lines when comparing the uncorrected to after the desaturation has been applied. Notably the separation of particle species at lower momenta and the separation of the Li species into ${}^6\text{Li}$ and ${}^7\text{Li}$, whereas there was little to no separation before.
255

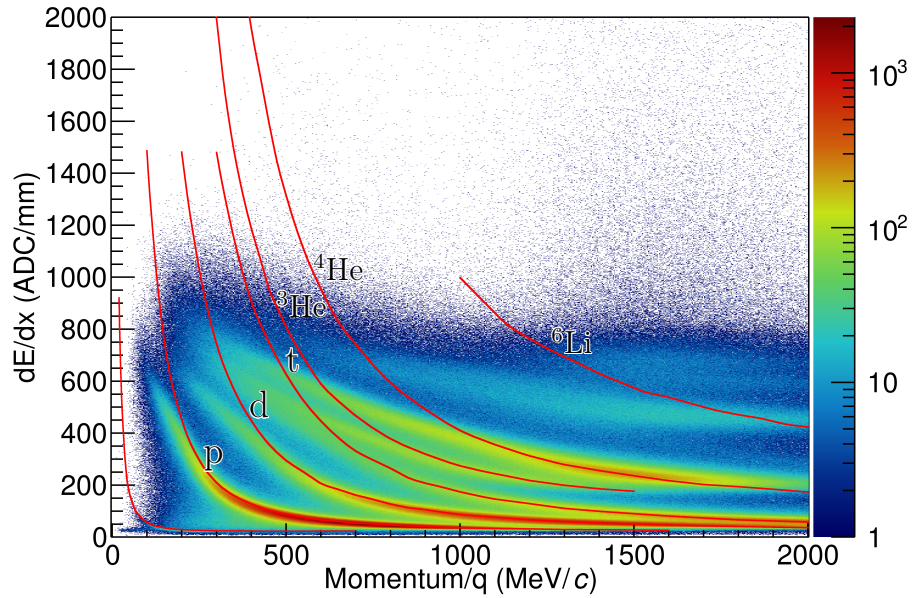


Figure 14: Uncorrected collision data.

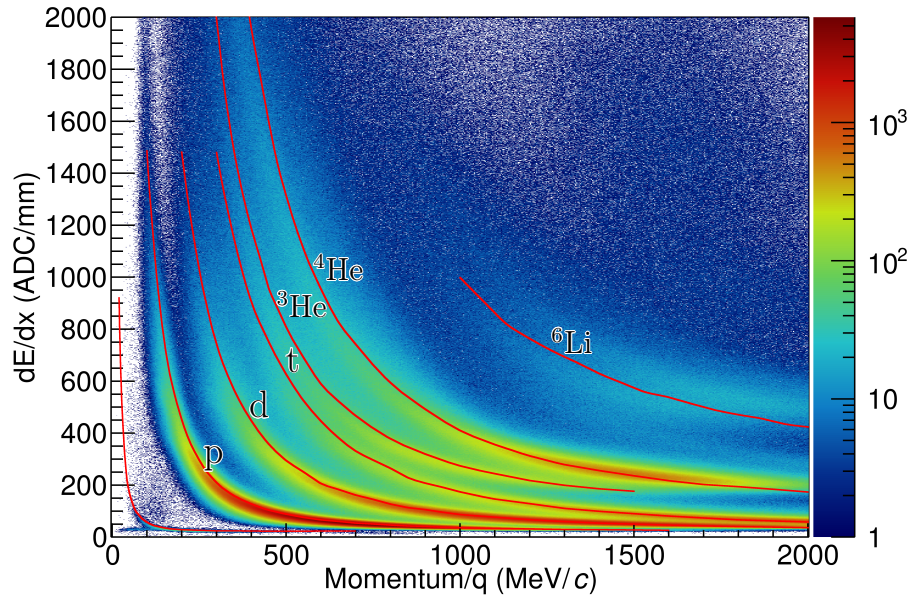


Figure 15: Corrected (desaturated) collision data.

260 **6. Conclusion**

The saturation of the electronics reduces dE/dx resolution and even the maximum charge observable inside of a TPC. We have shown that some of the saturation is recoverable. Since the Pad Response Function of the TPC is fixed by the anode wire geometries, an experimental PRF can be calculated from the unsaturated experimental data. The charge distribution resulting from an avalanche on a wire must follow this PRF even if the electronics of some channels directly under the avalanche are saturated. The pads further away are not saturated; by using these unsaturated pads we perform applying a χ^2 fit the unknown saturated pads to the known PRF.

270 Looking at the PID lines, and also making a direct comparison to some low gain sections of the TPC, we were able to extend the dynamic range of our electronics by a factor of about 5 times. This improved PID will allow for us to extend the momentum distributions of all species to lower momenta than what was previously available.

275 **7. Acknowledgments**

This work was supported by the U.S. Department of Energy under Grant Nos. DE-SC0004835, DE-SC0014530, DE-NA0002923, US National Science Foundation Grant No. PHY-1565546, the Japanese MEXT KAKENHI(Grant-in-Aid for Scientific Research on Innovative Areas) grant No. 24105004, and Polish National Science Center (NCN), under contract Nos. UMO-2013/09/B/ST2/04064 and UMO-2013/10/M/ST2/00624. The computing resources for analyzing the data was provided by the HOKUSAI-GreatWave system at RIKEN.

References

- [1] G. R. et. al., A tpc detector for the study of high multiplicity heavy ion collisions, IEEE Transactions on Nuclear Science 37 (2) (1990) 56–64. doi: 285 [10.1109/23.106592](https://doi.org/10.1109/23.106592).

- [2] R. S. et. al., S π rit: A time-projection chamber for symmetry-energy studies, NIM A 784 (2015) 513–517. doi:[10.1016/j.nima.2015.01.026](https://doi.org/10.1016/j.nima.2015.01.026).
- [3] S. et. al., A gating grid driver for time projection chambers, Nucl. Instr. Meth. Phys. Res. A 853 (2017) 44–52. doi:[10.1016/j.nima.2017.02.001](https://doi.org/10.1016/j.nima.2017.02.001).
- [4] E. P. et. al., Get: A generic and comprehensive electronics system for nuclear physics experiments, Physics Procedia 37 (2012) 1799–1804. doi:[10.1016/j.phpro.2012.02.506](https://doi.org/10.1016/j.phpro.2012.02.506).
- [5] M. A.-T. et. al., The fairroot framework, J. Phys.: Conf. Ser. 396 (2). doi:[10.1088/1742-6596/396/2/022001](https://doi.org/10.1088/1742-6596/396/2/022001).
- [6] C. H. et. al., A novel generic framework for track fitting in complex detector systems, Nucl. Instrum. Meth. A 620 (2-3) (2010) 518–525. doi:[10.1016/j.nima.2010.03.136](https://doi.org/10.1016/j.nima.2010.03.136).
- [7] W. Waltenberger, RaveâĂTa detector-independent toolkit to reconstruct vertices, IEEE Transactions on Nuclear Science 58 (2) (2011) 434–444. doi:[10.1109/TNS.2011.2119492](https://doi.org/10.1109/TNS.2011.2119492).
- [8] E. G. et. al., Optimum geometry for strip cathodes or grids in mwpc for avalanche localization along the anode wires, Nucl. Instr. Meth. Phys. Res. A 163 (1979) 83–92. doi:[10.1016/0029-554X\(79\)90035-1](https://doi.org/10.1016/0029-554X(79)90035-1).
- [9] W. Blum, W. Riegler, L. Rolandi, Particle Detection with Drift Chambers, Springer, Berlin, Heidelberg, 2008.